Journal of Neuroscience Methods 305 (2018) 89–97

Contents lists available at ScienceDirect

Journal of Neuroscience Methods

journal homepage: www.elsevier.com/locate/jneumeth

A simple, inexpensive method for subcortical stereotactic targeting in nonhuman primates

J. Nicole Bentley[a], Siri S.S. Khalsa[a], Michael Kobylarek[b], Karen E. Schroeder[b], Kevin Chen[a], Ingrid L. Bergin[c], Derek M. Tat[b], Cynthia A. Chestek[b], Parag G. Patil[a,b,*]

[a] Department of Neurosurgery, University of Michigan, Ann Arbor, MI, United States
[b] Department of Biomedical Engineering, University of Michigan, Ann Arbor, MI, United States
[c] Unit for Laboratory Animal Medicine, University of Michigan, Ann Arbor, MI, United States

ARTICLE INFO

Keywords:
Nonhuman primate
Image guidance
Stereotactic targeting
Subcortical targeting

ABSTRACT

Background: Many current neuroscience studies in large animal models have focused on recordings from cortical structures. While sufficient for analyzing sensorimotor systems, many processes are modulated by subcortical nuclei. Large animal models, such as nonhuman primates (NHP), provide an optimal model for studying these circuits, but the ability to target subcortical structures has been hampered by lack of a straightforward approach to targeting.

New Method: Here we present a method of subcortical targeting in NHP that uses MRI-compatible titanium screws as fiducials. The in vivo study used a cellular marker for histologic confirmation of accuracy.

Results: Histologic results are presented showing a cellular stem cell marker within targeted structures, with mean errors ± standard deviations (SD) of 1.40 ± 1.19 mm in the X-axis and 0.9 ± 0.97 mm in the Z-axis. The Y-axis errors ± SD ranged from 1.5 ± 0.43 to 4.2 ± 1.72 mm.

Comparison with existing methods: This method is easy and inexpensive, and requires no fabrication of equipment, keeping in mind the goal of optimizing a technique for implantation or injection into multiple interconnected areas.

Conclusion: This procedure will enable primate researchers to target deep, subcortical structures more precisely in animals of varying ages and weights.

1. Introduction

The ability to perform stereotactic targeting to various brain structures in large animal models has wide applicability across multiple areas of neurophysiologic, anatomic, and neuropathology research. For example, microelectrode recordings in cortical areas have enabled substantial progress in the development of brain-machine interfaces (Flesher et al., 2016; Gilja et al., 2012; Gilja et al., 2015; Hochberg et al., 2012; Hochberg et al., 2006; Jarosiewicz et al., 2015), have led to a better understanding of primary sensory (Ahissar et al., 1992; Gray et al., 1989; Maldonado et al., 2000) and motor systems (Riehle et al., 1997), and facilitated studies in stem cell transplantation (Lee et al., 2015) and tumorigenesis (Selek et al., 2014). However, there is a need to perform similar neurophysiologic and neuropathologic studies in subcortical areas as well (Buzsaki, 2004; Quiroga and Panzeri, 2009). While injection and implantation studies are widely performed in rodent models using atlas-based approaches (Bakhurin et al., 2016; Lin et al., 2006), the ability to use atlases for subcortical targeting in nonhuman primates (NHP) is limited by inaccuracies of this approach (Daye et al., 2013; Frey et al., 2004). Whereas rodent brain structures are relatively constant in size and location, NHP brains can be highly variable (Deogaonkar et al., 2005; Francois et al., 1996; Miocinovic et al., 2007), especially as the animal ages (Alexander et al., 2008; Koo et al., 2012; Matochik et al., 2000). Currently, much of the subcortical targeting being performed in NHP relies on histological (Paxinos et al., 1999; Saleem and Logothetis, 2012) or magnetic resonance imaging (MRI) atlases, in which up to 6 mm of anatomic variability in brain structures was seen (McLaren et al., 2009).

Acknowledging this anatomic variability, many laboratories have implemented other methods such as head-holding chairs (Frey et al., 2004), which requires extensive fabrication of bulky parts, or MRI-based targeting using non-ferrous compatible headframes (Bjarkam et al., 2009; Li et al., 2013; Chen et al., 2015). However, these MRI-compatible frames necessitate that the animal maintains its exact

* Corresponding author at: Department of Neurosurgery, University of Michigan, 1500 E. Medical Center Dr., SPC 5338, Ann Arbor, MI, 48109-5338, United States.
E-mail address: pgpatil@med.umich.edu (P.G. Patil).

https://doi.org/10.1016/j.jneumeth.2018.05.007
Received 24 August 2017; Received in revised form 10 May 2018; Accepted 12 May 2018
Available online 18 May 2018

position between imaging and surgery, a difficult task during transport, and is a limitation that introduces error. Additionally, use of these frames requires that imaging and surgery be performed in sequence, leading to long surgical and anesthetic times. As an alternative approach, skull-mounted cylinders or chambers are frequently used for single-unit subcortical recordings and enable serial electrode insertions (Galashan et al., 2011), but this technique is not conducive to multi-electrode array implantation, such as with macro-microelectrodes (Adtech, Racine, WA) or bundles of tungsten wires that require larger connectors or headstages. Due to these anatomic and procedural limitations, a method of individualized subcortical targeting is needed without the constraints of using specialized and expensive equipment. This is of special importance in large animal models, as there is a heightened need to mitigate risk from surgical procedures.

Here, a method is described that uses a simple, fiducial-based approach that is a substantial improvement over previous methods. It requires no customized parts or fabrication of devices, relies on widely available equipment, is inexpensive, and is easily adapted to any laboratory with MRI access. Briefly, the method involves implantation of MRI-compatible titanium screws around the skull in a minor procedure. The screws serve as fiducials, which are uniquely defined, immobile reference points that can be located both in physical space and imaging space. Importantly, fiducials must be distributed widely over the skull due to the creation of a centroid by their configuration, the center of which should approximate the target as closely as possible. Co-registration of imaging and surgical spaces is then performed, which enables the selection of a target on the image and the transformation of its coordinates into surgical coordinates. Results are presented from an in vivo application using a cellular marker for histologic confirmation of targeting accuracy, with a discussion of the elements that were crucial for success.

2. Materials and methods

2.1. Animals

All animal experiments were performed in accordance with animal use protocols submitted to and approved by the University of Michigan Institutional Animal Care and Use Committee. All animals were rhesus macaques at the end of their experimental lifetimes for other studies. Two NHP had deep structures targeted with stem cell injections: 2 injections were performed in Monkey F (19-year-old male, 12.6 kg; thalamus, hippocampal injections) and 6 were performed in a second animal, Monkey B (25-year-old female, 8.4 kg; bilateral thalami, hippocampi, and substantia nigra injections). An additional 10 animals (aged 5–32 years) at their experimental endpoints and that were otherwise to undergo euthanasia were used for optimization of fiducial design, MRI parameters, and surgical technique. One of these 10 animals (Monkey S; 20-year-old male, 12.5 kg) had data available for comparison of atlas-based and MRI-based approaches using a slightly different technique, prior to optimization of this method.

2.2. Fiducial placement

The overall technique begins with fiducial placement. After several design iterations, the optimal markers were self-drilling titanium screws (Biomet HT X-drive screw #95-6104, Warsaw, IN) measuring 1.5 mm in diameter and 4 mm in length. The implantation procedure was begun by first sedating the animal with telazol 4 mg/kg intramuscular (IM). The animal was then intubated and sedation maintained using gas anesthesia (isoflurane 1.25–3%). Titanium screws were implanted in a procedure lasting approximately 20 min, and the animal was imaged with MRI immediately following this, with imaging lasting approximately 45 min. Additional time was needed for transport to an off-site MRI scanner, totaling approximately 2-2.5 h for the entire procedure. Additional analgesia was given postoperatively using carprofen (2 mg/kg) subcutaneously, given at 12 and 24 h.

The fiducial implantation procedure began with the animal in the prone position and the head supported on a stack of towels. To facilitate visualization, the head was first shaved. Betadine was used for antisepsis at the desired fiducial sites. Sterile drapes were applied around the head and the scalp was infiltrated with bupivicaine 2.5% with epinephrine 1:200,000 for local anesthesia at the proposed sites of implantation. Antibiotics were administered prior to incision (cefazolin 25 mg/kg). Fiducial locations were bilateral supraorbital ridges, two pairs of parietal sites bilaterally (asymmetrically placed), bilateral occipital nuchal ridges, and bilateral zygomatic roots just anterior to the external auditory meatus. The first site of fiducial placement was incised via a stab incision using a #15 surgical blade. The bone was cleared of soft tissue and periosteum using blunt dissection with a 4 × 4-cm gauze on the end of a hemostat. Once the bony surface was cleared of tissue, a drill bit (Biomet 1.5-mm HT X-lock short-drive blade #15-1194, Warsaw, IN) was used to implant a self-drilling screw with a hand-held screwdriver until flush with the skull surface (Biomet twist-drill handle #01-7390 or #01-7164, Warsaw, IN). Following placement, the skin incision was closed over the screws with a non-absorbable monofilament nylon suture (1–2 sutures per site, using 3-0 Ethilon©, #1673H, Ethicon, Somerville, NJ). Alternatively, an entirely subcutaneous closure could be performed using an absorbable monofilament suture, such as a 4-0 Monocryl© (#Y218H Ethicon, Somerville, NJ), using a subcuticular stitch. This process was repeated for the remaining fiducial locations.

The most challenging screws to place were at the zygomatic roots and external occipital protuberances. The zygomatic root can be palpated on the skin and is defined as the superior and anterior border of the external auditory meatus, which provides a relatively flat plane for screw placement as it slopes upward to and is continuous with the squamous temporal bone. The skin incision was made overlying this prominence, and the dissection was directed through deeper layers of muscle until the bone was reached. Though not required, monopolar electrocautery can be used to clear the bone of temporalis muscle and to provide hemostasis. The external occipital protuberances serve as attachment sites of the occipital musculature and are also easily palpated on the scalp. Incisions were made over these bilaterally, off of midline, and blunt dissection was used to clear the bone of soft tissue using a hemostat and gauze. Additional fiducials may be implanted over the head as needed, keeping in mind that asymmetric placement over the head will ensure confirmation of side on imaging.

The procedure in Monkey S was similar to this optimized procedure, however, screws were housed in a plastic anchor and fiducial locations did not include zygoma and occipital protuberances.

2.3. Imaging

Following fiducial placement, an MRI was obtained, however, there is no requirement that the fiducial implantation and imaging be performed the same day, as fiducials are entirely implanted and do not dislodge from the bone. For an independent imaging session, sedation can be administered with intermittent bolus doses of telazol IM (4 mg/kg). If being performed on the same day as the definitive procedure, inhaled or continuous IV anesthetic can be given using a portable MRI-compatible ventilator (ModuFlex Compact SN 4086, Dispomed, Joliette, Quebec, Canada) with an isoflurane vaporizer (InterMed Penlon Sigma Delta SN D0610 0110, Penlon Limited, Abingdon, Oxon, United Kingdom).

Animals were positioned supine on the MRI table. During the procedure, the animals' heart rate, respiratory rate, and oxygen saturation were monitored. Imaging was performed at our institution on a General Electric® MR750 3.0 T system using primarily a sagittal T1-weighted image (flip angle 12, echoes 1, TI 450, bandwidth 31.25, FOV 19.2, slice thickness 0.5 mm, 384 × 384 matrix, NEX 2, phase FOV 1). Screws are more easily seen on T1 imaging, however, in order to maximize

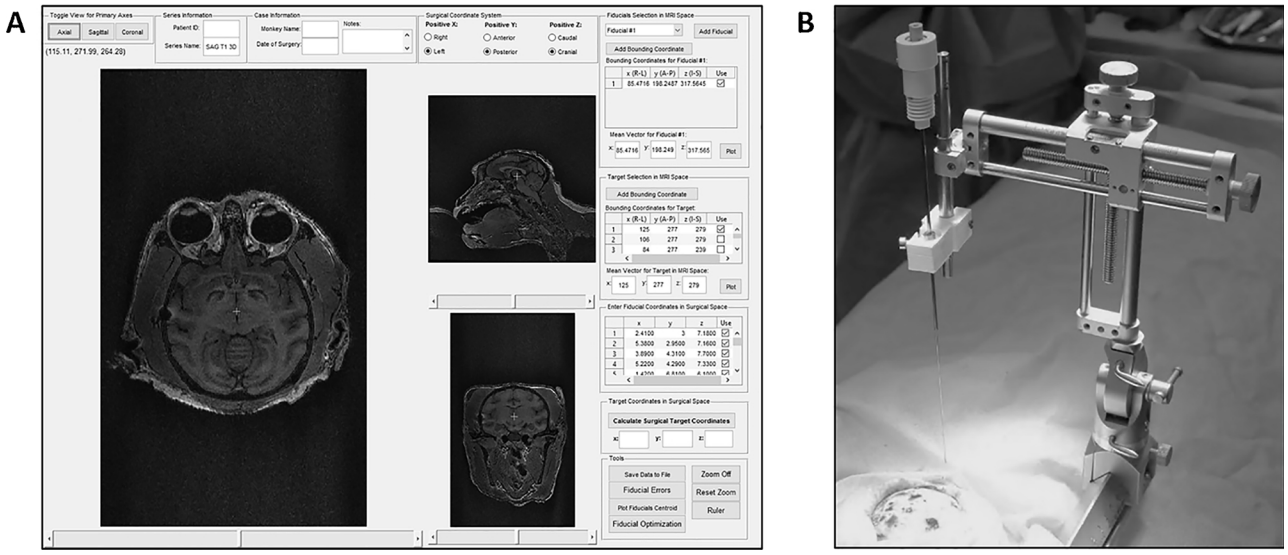

Fig. 1. Stereotactic localization. **A:** Graphical user interface to visualize, record, and calculate coordinates and transformation matrices from the MRI. **B:** Surgical setup to localize fiducial markers with a stereotactic arm and localizing cannula.

visualization of subcortical nuclei, T2-weighted images could also be obtained and merged to T1 images.

2.4. Co-registration of imaging to frame-based coordinates

After the MRI was performed, images were uploaded into a DICOM viewer for operative planning. For automation of both image viewing and coordinate transformation, a MATLAB (MathWorks, Natick, MA) graphical user interface (GUI) was created (Fig. 1**A**), though any software providing unique coordinates would be sufficient, such as Analyze 12.0 (AnalyzeDirect, Inc., Overland Park, KS) or OsiriX (Pixmeo, Bernex, Switzerland). The titanium screws create a metal artifact visualized as an approximately 5-mm-diameter void on T1 imaging on a 3 T magnet. The center of the void corresponds to the center of the screws, found easily both in MRI and during surgery. The X-, Y-, and Z-MRI coordinates of screw centers were recorded for later registration. In addition to identification of fiducials, target points of desired subcortical structures were also chosen on the MRI. Once the subcortical structures' coordinates were determined, animals then underwent the stem cell injection procedure.

Animals were sedated with telazol 4 mg/kg and transported to the operating suite where general anesthesia was induced and animals were endotracheally intubated. A surgical plane of anesthesia was maintained with isoflurane. After insertion of a peripheral IV and a bladder catheter, animals were positioned prone in a standard primate headframe (Kopf Model 1430, David Kopf Instruments, Tujunga, CA). The scalp was shaved and cleansed with an antiseptic solution of betadine, and a surgical field was created with sterile drapes. Analgesia was provided with local injection of bupivacaine 2.5% with epinephrine 1:200,000 and a continuous infusion of fentanyl (5–10 mcg/kg/hr). Depending on experimental needs, each previous stab incision can be opened to visualize the screws, or a single midline incision can be made, and the scalp reflected laterally to expose all fiducials at once. Following incision, the first step was to register fiducials in the surgical space to MRI space using a stereotactic arm (Kopf Model 1460, David Kopf Instruments, Tujunga, CA) attached to the headframe. A localizing cannula was positioned over the center of the screws, and the surgical X-, Y-, and Z-coordinates of each fiducial were read from the headframe and arm (Fig. 1**B**).

It is important to maintain the same direction and handedness as the MRI in all axes, as the transformation matrix consists of rotation and translation. Once all coordinates were known, they were used to calculate an affine transformation (Hartov and Roberts, 2009) in MATLAB (code provided in **Appendix A;** a standalone program is available upon request). Importantly, the affine transformation incorporated the appropriate scale factors as determined in MRI space, and which were different for each axis. The transformation produced a rotation matrix and translation vector that were combined in a 4 × 4 transformation matrix that was then applied to chosen target points on the MRI to produce a solution for the coordinates in surgical space. With registration to frame space complete, the stereotactic arm was moved to the X- and Y-coordinates of the target entry site. If not already incorporated into the surgical field and incision, this area would be shaved, prepped, and draped. An opening in the skull of any desired size could be drilled to accommodate a cannula or other delivery device, but for our purposes, we used a handheld air-powered drill (Midas Rex EM200 Legend high-speed drill; Medtronic, Minneapolis, MN) to make a small craniotomy

2.5. In vivo confirmation

To confirm placement, stem cells (HK532.UbC-IGF1; NeuralStem, Rockville, MD) were injected that could be easily localized in histologic sections without the need for special stains. For the injections, hydraulic tubing attached to the injection device (Intracerebral Microinjection [IMI] device; FHC, Bowdoin, ME) was first filled with hibernation media by using the "REFILL" function of a syringe pump (PHD 2000; Harvard Apparatus, Holliston, MA). The hydraulic line measured 2.5 m with an ID of 0.019" for a fill volume of approximately 0.45 mL. Stem cells were backfilled into the tubing, initially at a volume of 70 µL. The IMI device was positioned over the first entry site. A small stab incision was made in the dura and pia with a #11 scalpel to allow smoother passage of the blunt-tipped instrument. The IMI device was first painted with tissue dye (Davidson Marking System tissue marking dye, cat #2401-P, Bradley Products, Bloomington, MN) to mark the entry site for later histologic sectioning, and was then lowered slowly to the desired depth using the stereotactic arm (Kopf Model 1460, David Kopf Instruments, Tujunga, CA). The pump was set to a target volume of 20 µL and an initial rate of 2 µL/min. Cells were injected over a 1-minute period, followed by a settling time of 2 min to reduce diffusion (Gutierrez et al., 2015). After injection, the IMI was retracted, and once all locations had been injected, the animal was then euthanized using sodium pentobarbital (390 mg/mL, 1 mL/4.5 kg), and the brain was harvested for histologic analysis.

The injection procedure for Monkey S included implementation of the MRI-based approach described here for a hippocampal site in the left hemisphere, and an atlas-based approach of a corresponding site in the right hemisphere. Atlas coordinates were obtained (Saleem and Logothetis, 2012) and used to localize an entry site in the right hemisphere of the animal as it was secured in the standard headframe, using ear-bar zero (EBZ) as the reference. The coordinates were independently verified by three investigators to confirm accurate localization.

2.6. Fixation method

Following euthanasia, the brain was harvested and immersion fixed in a 10:1 vol of 10% neutral buffered formalin (3.7% formaldehyde) for 15 (Monkey B) or 36 days (Monkey F). A board-certified veterinary pathologist performed all sectioning by adaptation of standard trimming guidelines for nervous system sampling in primates (Pardo et al., 2012). An initial coronal cut was made manually with a Thomas Scientific tissue blade (6727C18, Thomas Scientific, Swedesboro, NJ) by placing the dorsal cortex on the cutting surface and angling the frontal lobe approximately 20 degrees to the benchtop, corresponding to the orientation of the MRI coronal sections in relation to the brain. Following the initial cut, gross sectioning was performed at a standard 4-mm thickness in the coronal plane in preparation for histology, cassetting, and paraffin-processing, using a gross trimming matrix manufactured at a 4-mm thickness. This method follows previously published industry standard techniques (Pardo et al., 2012). Sections thinner than 4 mm are generally not recommended due to tissue degradation or damage during paraffin infiltration. Coronal sections were numbered from the rostral pole of the brain (e.g., the initial 0–4 mm is “Section 1”) and were verified against coronal MRI sections corresponding to the same location.

The 4 mm-thick coronal gross sections, containing the known targeted landmarks, as visualized grossly (thalamus, hippocampus, and substantia nigra), were placed into cassettes for paraffin embedding. For each cassette, 4-μm-thick sections were cut from one face of the 4 mm tissue using a microtome. These were cut at a total of 3 levels, separated by 25 μm, covering a total of ~160 μm for each cassette. For all blocks, one of the three sections at each level was stained with hematoxylin and eosin for evaluation, and the other two were left unstained for future staining or immunohistochemistry. For some blocks, the embedded tissue was melted down and re-embedded in the opposite orientation (anterior versus posterior face) and the process was repeated, to localize whether cells were present at both ends of the 4 mm thickness embedded section.

2.7. Histologic evaluation of accuracy

All measurements refer to fixed tissue, which has some shrinkage compared to unfixed tissue. To determine targeting accuracy, the MRI targets used during the surgical procedure were visualized on the DICOM viewer or GUI. The target coordinates were defined, as were the coordinates of easily identifiable landmarks. Distances from the target points to the landmarks were calculated by subtracting the coordinates and multiplying by the appropriate scale factors, converting MRI coordinates to millimeters. The landmarks corresponded to the midline in the mediolateral plane (X-axis) for all injection sites. For dorsoventral (Z-axis) measurements, measurements were taken to the closest easily identifiable landmark as follows: hippocampal sulcus for hippocampal injections and the ventral aspect of the cerebrum for substantia nigra and thalamic injections (corresponding to the cerebral crus). Histologically, the geometric center of cellular aggregates was identified, and measurements were made to the landmarks in the X- and Z-axes corresponding to those visualized on MRI. The final error was calculated as the difference between the MRI and histologic measurements. A blinded veterinary pathologist performed histologic measurements and the primary experimenter performed MRI measurements. Y-axis measurements were inherently less precise because, unlike other planes where landmarks could be measured on the same slice in the sectioned plane, true measurements could be made only by totaling the sections between. Due to this, accuracy measurements in the Y-axis are reported to the limits of calculated slice thicknesses. For cells that were identified on the rostral or caudal face of the section, but not the face of the next section, accuracy could be estimated to the limits of the slice thickness, or 4 mm. For other sections where cells were identified within the slab of tissue (left and right substantia nigra), more precise estimates could be made after totaling microtome sections. Therefore, Y-axis measurements are reported as a range spanning the least possible to largest possible errors. All measures of overall error are reported as mean ± standard deviation (SD) of the root-mean-squared errors.

3. Results

3.1. Comparison of atlas- and MRI-based approaches

Prior to implementation of Biomet screws as fiducials, this method was employed in one animal (Monkey S) that illustrates the difference between surgical coordinates using these approaches, though histologic confirmation with stem cells was not possible. The MRI-based method localized an entry site over the left hemisphere near the central sulcus (Fig. 2**A**), while the atlas-based method localized the entry in the occipital lobe on the right (Fig. 2**B**), the coordinates of which were independently verified by three different investigators. While cellular aggregates were not visualized in this experiment and distance measurements were not obtained, evidence of successful hippocampal localization was confirmed on the left with a small hemorrhage and served to illustrate the large disparity between the two approaches.

3.2. Fiducial placement

The configuration of fiducials created a centroid as described mathematically in Appendix B. The optimal configuration was that in which the centroid was located at the target itself; however, for deep subcortical structures, this required that fiducials be placed more inferiorly than was feasible using a standard headframe and stereotactic arm. By examining the target registration error (TRE; Fig. 3), it was determined that placement of screws over the convexities alone resulted in an estimated TRE of 1.5–2 mm at a chosen target in the hippocampus. In contrast, widely variable distribution in all 3 axes resulted in an inferiorly displaced centroid in which the TRE was within 0.8 mm.

3.3. Imaging results

The titanium screws were imaged as previously described, creating an approximately 5-mm artifact visualized on MRI as a circular void. These markers are shown in Fig. 4**A** in arbitrary positions in a cadaveric specimen as well as in vivo on MRI. The superior center of this void in the axial, sagittal, and coronal projections corresponds to the center of each marker **(**Fig. 4**B)**.

3.4. Targeting results

To confirm targeting accuracy using this method, neural stem cells were injected that could be identified histologically. Injections in Animal F targeted unilateral thalamus and hippocampus, and injections in Animal B were performed in bilateral thalami, hippocampi, and substantia nigra. Among the 8 attempted injections, 1 had no histologic correlate due to technical failure of the injection apparatus. Histologic results of injections are shown in Fig. 5, with easily visualized cells seen within the targeted structures.

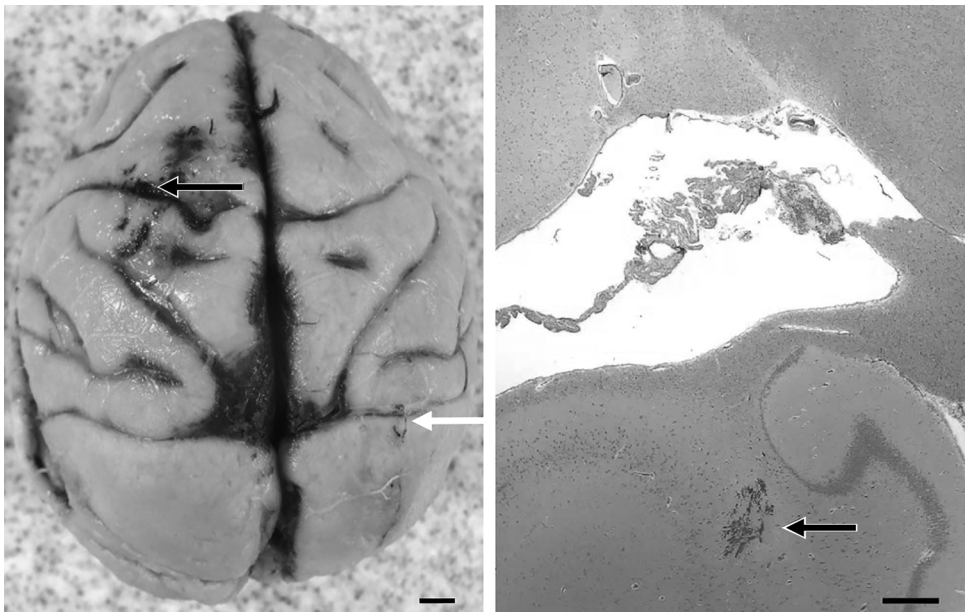

Fig. 2. Comparison of MRI- and atlas-based entry site localization. **A:** Whole brain specimen revealing location of intended hippocampal targeting using MRI-based method, with entry site near central sulcus (black arrow), and atlas-based method, with entry site in occipital lobe (white arrow). Scale bar = 5 mm. **B:** Histologic specimen showing hemorrhage within the left hippocampus (black arrow) using the MRI-based approach; no histologic correlate was found in the right hemisphere. Scale bar = 500 u m.

In a secondary analysis, we attempted to quantify the amount of error between the targeted site as defined on MRI and the site of histologically identified cells. Based on measurements described in the Methods section, the mean errors ± SD were 1.40 ± 1.19 mm in the X-axis and 0.9 ± 0.97 mm in the Z-axis. In the Y-axis, because gross specimens were sectioned in the antero-posterior plane, estimates of mean error are calculated as a range, with a minimum of 1.5 ± 0.43 mm and maximum of 4.2 ± 1.72 mm. Fig. 6 shows the individual error measurements obtained for each axis, and all individually measured errors are shown in Table 1.

4. Discussion

Primate models are ideal for many neurophysiologic and neuroanatomic studies, however, research in these areas has been hampered by an inability to accurately target deep, subcortical nuclei using the animal's own MRI instead of relying on primate atlases. Unlike rodent or other small animal models in which brain structures are largely

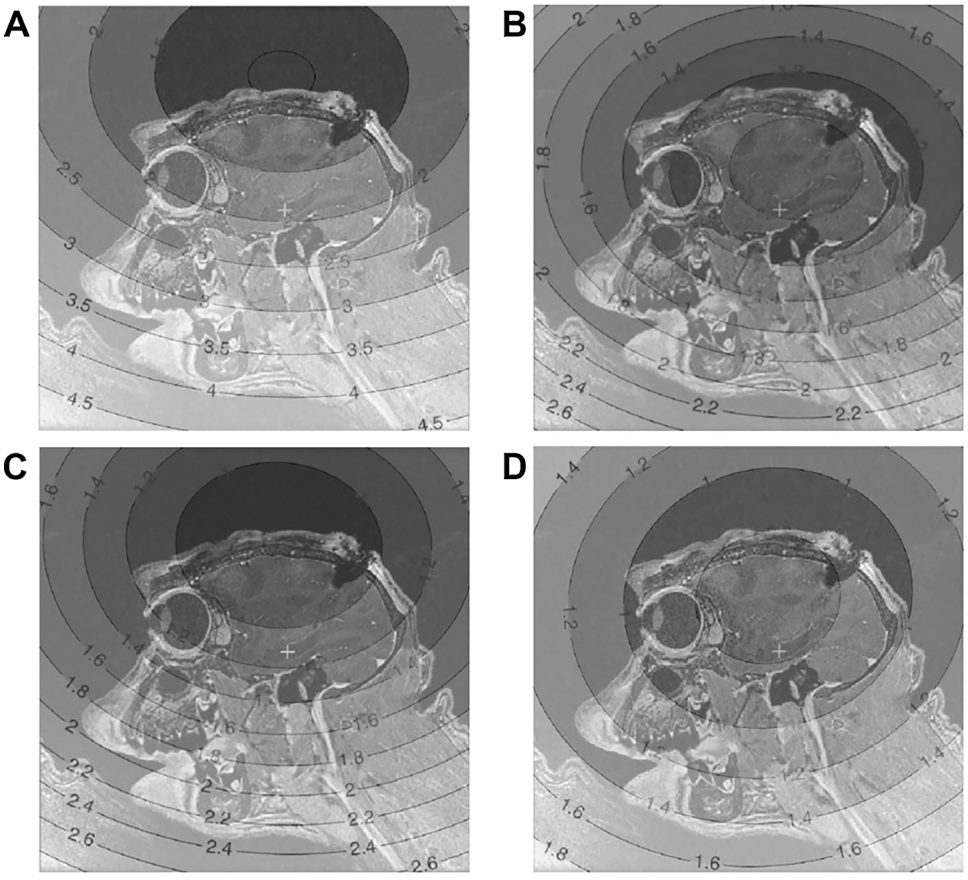

Fig. 3. Contour plots of target registration error (TRE) in millimeters for four fiducial configurations. The target is identified with the '+' symbol. **A:** Fiducials are located exclusively on the top of the head, yielding isocontours that increase more rapidly, resulting in a TRE at the target between 1.5–2 mm. **B:** Fiducials are dispersed around the head, including the top and sides, resulting in a more inferior centroid and isocontour lines that increase less rapidly. **C:** Fiducials at the top, anterior, and posterior head, resulting in isocontour lines that increase less rapidly but have a TRE 1–1.2 mm at the target. **D:** Fiducials limited to the top and lateral aspects of the head, resulting in wide isocontours of low TRE, such that the TRE at the target is < 0.8 mm.

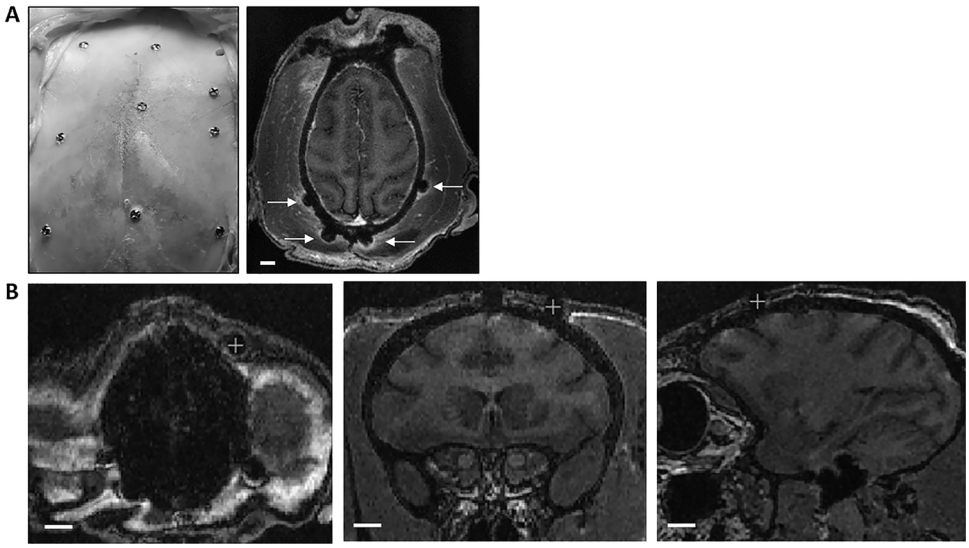

Fig. 4. MRI-based targeting method. **A:** 1.5 × 5-mm titanium surgical screws (left), screw fiducials in a cadaveric specimen in arbitrary positions (middle), and MRI appearance of screws in vivo (right). **B:** MRI appearance of fiducials in axial (left), sagittal (middle), and coronal (right) planes. Screws denoted by crosshairs. Scale bars = 5 mm.

constant between animals, primate (i.e., NHP and human) brains show greater structural variability (Deogaonkar et al., 2005; Francois et al., 1996; Miocinovic et al., 2007). This variability is even greater in older animals, necessitating that age be carefully considered when performing targeted injections or implantations (Alexander et al., 2008; Koo et al., 2012; Matochik et al., 2000). Therefore, while atlases are sufficient for targeting in small animals, the precision needed to target subcortical nuclei in primates requires that a more subject-specific approach be taken, highlighted in the present study by the difference in injection sites between MRI- and atlas-based methods, as shown in Fig. 2.

Two primary alternatives exist for individualized targeting: deformable atlases and fiducial-based co-registration. Deformable atlases rely on a model MRI that can be re-scaled and warped so that individual nuclei are aligned, such as in Miocinovic, et al. (2007). However, this and other MRI-based atlases frequently use a "standard" MRI created from either one or several averaged images, limiting the generalizability of anatomic locations to individual animals (McLaren et al., 2009, Miocinovic et al., 2007). For example, in developing a population-averaged MRI atlas, up to 6 mm of variability was found in superficial structures, and over 2 mm of variation was seen in deep nuclei (McLaren et al., 2009). When considering error introduced by the targeting procedure itself, this margin could easily result in significant inaccuracy.

As an alternative to atlases, co-registration of an individual animal to its MRI using fiducials has been a well established approach for several decades (Perry et al., 1980), and has evolved into sophisticated frameless technologies in humans (Henderson, 2009). However, use of similar equipment in primate research is prohibitively expensive for many laboratories and is cumbersome to use. One commercially available system uses a skull-mounted fiducial array and optical tracking for frameless navigation (Brainsight®, Rogue Research, Montreal, Quebec, Canada). While an elegant solution, optical tracking is of significant expense. Of arguably more importance is the fiducial array design, which limits the 3-plane variability over the skull. As shown in Fig. 3 and explained in detail in Appendix B, restriction of fiducials to a

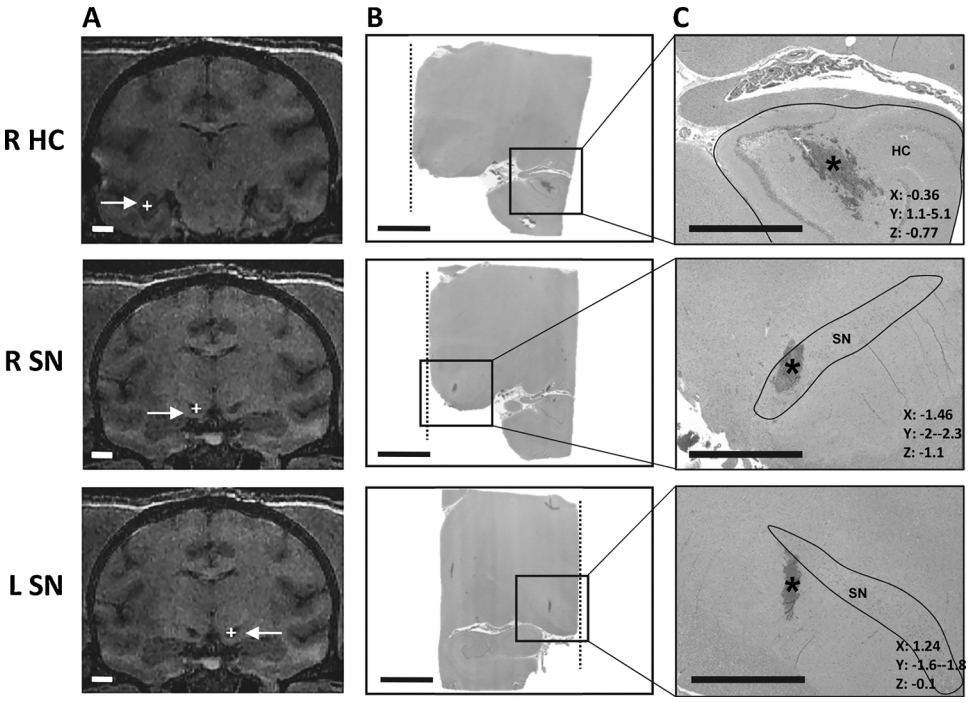

Fig. 5. Targeted areas on MRI (left) of 3 of 7 injection sites with histologic confirmation (middle, right) **A.** MRI appearance of target (white arrow); **B.** Histologic appearance of cell aggregates in target structures ; **C.** Magnification of insets in B. Asterisks (*) denote injected stem cells. Scale bars = 5 mm (left), 6 mm (middle), 2 mm (right). Abbreviations: HC, hippocampus; SN, substantia nigra.

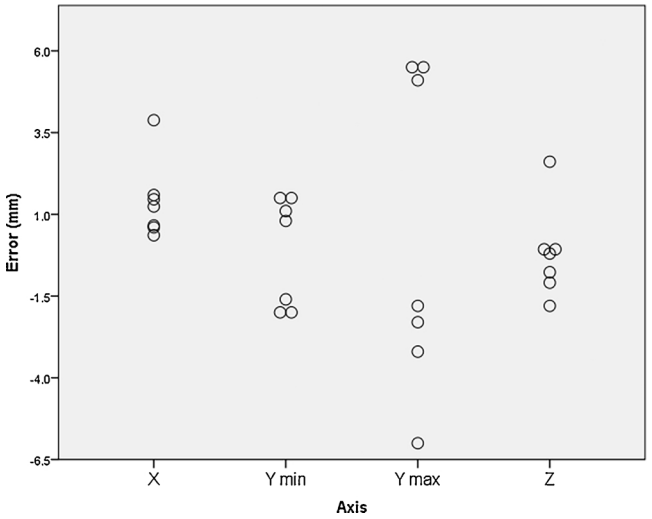

Fig. 6. Scatter plot for error measurements obtained in each axis for 7 total injections. The Y-axis is represented as a minimum and maximum due to sectioning technique, as described in the Methods section.

Table 1
Individual injection error measurements for two animals in three planes.

Structure	X[a]	Y min	Y max	Z
Animal B				
R SN	−1.46	−2.00	−2.30	−1.09
L SN	1.24	−1.60	−1.80	−0.07
L Thal	1.59	1.50	5.50	−0.20
R HC	−0.36	1.10	5.10	−0.77
L HC	−3.88	1.50	5.50	−0.07
Animal F				
L Thal	−0.66	0.80	−3.20	2.61
R HC	−0.60	−2.00	−6.00	−1.80

Abbreviations: SN: substantia nigra; HC: hippocampus; Thal: thalamus.
[a] all measurements given in millimeters.

small area constrains the centroid they create (Fitzpatrick et al., 1998), leading to rapid loss of accuracy at the target. As a precursor to the Brainsight® system, Frey, et al. (2004) introduced a fiducial-based approach that used skull-mounted fiducial pegs and a custom head-holding chair. Again, centroid creation is limited in its inferior extent, and the use of custom equipment limits adaptability. Additionally, the implanted pegs seemed to be exposed in the scalp, presenting a relative hazard to the animal if dislodged.

Similar to the head-holding chair, other types of head immobilizers (White et al., 2011) and frame adapters (Bjarkam et al., 2009; Chen et al., 2015; Li et al., 2013) exist, each requiring fabrication of various complex parts. Simpler fiducial-based designs have been used for several decades, and have included implanting contrast-filled glass beads (Alvarezroyo et al., 1991; Rebert et al., 1991) and drilling into the animals' incisors (Walbridge et al., 2006). In addition to creating a small centroid, these procedures also require a separate anesthetic and placement into a headframe, whereas the technique presented here is performed under mild sedation in a procedure room.

Perhaps the most widely used method of stereotactic targeting is with an MRI-compatible headframe (Baker et al., 1999; Barua et al., 2013; Dubowitz and Scadeng, 2011; Katnani et al., 2016; Knight et al., 2013; McBride and Clark, 2016; Rebert et al., 1991; Saunders et al., 1990; White et al., 2011). This headframe obviates the need for subsequent coordinate transformation, as there is a direct relationship between imaging and surgical spaces. While it does simplify the workflow, it requires that imaging and the definitive procedure be performed in series, with no movement of the animal in between, which would result in a frameshift of coordinates. This complete immobilization is a significant limitation when transporting between rooms or facilities, and even very small perturbations that may go unnoticed will alter targeting accuracy. Furthermore, stereotactic planning can only be performed after images have been obtained, increasing total anesthetic and procedural times, resulting in greater risk to the animal. Finally, many MRI scanners do not have sufficient bore diameter to accommodate the large size of the compatible headframe, further limiting widespread adaptability.

In the currently presented method, we have attempted to overcome the drawbacks discussed in each of these systems. Regarding the fiducials themselves, we found that surgical-grade, widely available titanium screws are economical and fully implantable. They have been used similarly in human neurosurgical procedures (Aldana et al., 2010; Thompson et al., 2011), ensure no movement after implantation, and are fully covered by scalp, presenting low risk to the animal. They can be implanted in a minor procedure under mild sedation (e.g., ketamine) and local anesthetic in any position that provides access to the head. This flexibility in positioning enables implantation to be performed in a procedure space rather than in a more expensive OR setting, and does not require fixation in a headframe.

The sites of implantation have been optimized here to create a centroid with low estimated error at deep nuclei. By placing fiducials more inferiorly, the centroid is displaced downward, closer to the desired target. Unfortunately, the commonly used primate headframes limit accessibility to the inferior aspect of the head, but the zygomatic roots and inferior occipital protuberances provide sufficient Z-axis coverage, and the screws can be implanted in a variety of areas depending on specific needs. Additionally, due to their small size, these fiducials can be easily be used for cynomolgus macaques, porcine, sheep, or other models, as evidenced by their implementation in animals of significantly different ages and sizes.

Regarding imaging, this method enables scanning in virtually any position, without the need to immobilize the animal in a specific orientation or to center the images on specific structures, such as the anterior and posterior commissures. The size of the magnet's bore is not a limitation with this technique, and imaging can be done at any time before the definitive procedure, reducing anesthetic time to the animal and allowing for pre-surgical planning prior to the procedure. After identification of the fiducials in MRI space, co-registration requires only that stereotactic surgical coordinates can be obtained in a process that takes 15–20 min and is easily performed using widely available standard headframes (e.g., Kopf Model 1430, David Kopf Instruments, Tujunga, CA). Fiducials are located in surgical space by opening the scalp over them, and a simple coordinate transformation is performed (see Appendix A), providing target coordinates. Once the surgical procedure is complete, the screws may be easily removed or left in place.

In optimizing technique, accuracy must not be compromised. Here, we chose to illustrate feasibility and accuracy using injections of neural stem cells that could be visualized histologically. Using this method, we calculated errors (mean ± SD) of 1.40 ± 1.19 mm in the X-axis, between 1.5 ± 0.43 mm and 4.2 ± 1.72 mm in the Y-axis, and 0.9 ± 0.97 mm in the Z-axis. These errors are within the range necessary to target small subcortical nuclei, and therefore this method will be applicable to any experimenter performing deep stereotactic injections in a large animal model. As such, this will be an important technique for neurophysiologists performing deep single- or multi-unit microelectrode recordings or for targeted implantations of microelectrode arrays or deep brain stimulators for continuous chronic recordings. The method is also ideal for experimenters performing stereotactic injections of stem cell or viruses for gene therapies or optogenetic studies.

We acknowledge several limitations of this design and the results presented here. Regarding the technique itself, targeting is currently constrained to orthogonal planes. Some targets of interest may be surrounded by cerebrospinal fluid space, vascular, or eloquent structures

that require an oblique trajectory, for which this method has not been designed. An additional limitation encountered when performing intraparenchymal injections or implantations is the occurrence of tissue compression. When inserting a device of any kind, the device itself depresses and compresses the immediately surrounding tissue (Sridharan et al., 2013). This unpredictable distortion also leads to inaccuracies, and the present work does not have a specific method of mitigating this. Additionally, use of bolts or cannulas that permit entry of injections or devices would be ideal, and this is a likely an area for further refinement in future studies.

Regarding the study methodology, we acknowledge several limitations. First, estimates in the Y-plane are inherently imprecise due to the sectioning technique, as described in the Methods section. Additional confirmation with MRI would further support histologic measures, but would require an MRI-visible marker of injection, which we have not yet implemented. Also, results of a direct comparison were available in only one animal, with the clearly inaccurate atlas-based entry site localizing to the occipital lobe. Though cells were not visible histologically, hemorrhage in the hippocampus did support successful MRI-based targeting. Future studies of direct comparisons would further confirm the improved accuracy of this method, however, we believe that the procedural improvements alone (ability to perform sessions on different days, variable headframe positioning, etc.) support use of this technique. Here, we targeted the hippocampus due to its widespread study in neurophysiologic investigations, and the substantia nigra due to its small size. Though this study is limited to these structures, an ability to target the substantia nigra with a low error in bilateral hemispheres exemplifies the method's usefulness in targeting any chosen subcortical area. A further limitation of this specific method is that MRI must be performed with parameters similar to what is used for clinical imaging, and research scanners with lower resolution would likely not be able to display the screw artifact sufficiently.

5. Conclusions

This report describes an easy, inexpensive, and adaptable technique that can be used for chronic population recordings or intraparenchymal injections into multiple, deep, interconnected brain areas. Technology for performing these recordings is also becoming more accessible (Patil et al., 2004), and increasingly complex methods of analyzing the expansive data sets are also evolving (Baccala and Sameshima, 2001; Chen et al., 2006; Cunningham and Yu, 2014; Kaminski et al., 2001; Kaminski and Blinowska, 1991). All of these goals are driven by the need to understand neuronal function both in normal and pathological states, and though the importance of this has long been acknowledged, the process by which we may combine these tools is now becoming increasingly available.

Author contributions

P.G.P., C.A.C., and J.N.B. designed research; J.N.B., K.E.S., K.C., and M.K. performed surgeries; I.B. and J.N.B. performed necropsies; J.N.B., S.S.S.K., D.M.T., I.B., P.G.P., and C.A.C. analyzed data; J.N.B., S.S.S.K., M.K., K.C., I.B., P.G.P., and C.A.C. wrote and revised the paper.

Conflicts of interests

The authors declare no conflicts of interest.

Acknowledgements

This work was supported by a grant from the A. Alfred Taubman Medical Research Institute. The authors wish to thank the Animal Care and Use Program and Unit for Laboratory Animal Medicine for assistance in surgeries and animal care. We thank Kaile Bennett and Eric Kennedy for animal care and training, and the histology and necropsy technicians of the ULAM In Vivo Animal Core for histological preparations. We also thank the Functional MRI Laboratory at the University of Michigan, and Neuralstem and the Feldman Lab for providing neural stem cells. We also thank the Shih Lab for assistance in 3D printing and Tom Cichonski for editorial review.

Appendix A. Supplementary data

Supplementary material related to this article can be found, in the online version, at doi: https://doi.org/10.1016/j.jneumeth.2018.05.007.

References

Ahissar, M., Ahissar, E., Bergman, H., Vaadia, E., 1992. Encoding of sound-source location and movement: activity of single neurons and interactions between adjacent neurons in the monkey auditory cortex. J. Neurophysiol. 67, 203–215. http://dx.doi.org/10.1152/jn.1992.67.1.203.

Aldana, P.R., MacGregor, T.L., James, H.E., Marcus Jr., R.B., Indelicato, D.J., 2010. Titanium screws as fiducial markers for image-guided stereotactic proton irradiation in pediatric central nervous system tumors: a technical report. Pediatr. Neurosurg. 46, 227–231. http://dx.doi.org/10.1159/000320147.

Alexander, G.E., Chen, K., Aschenbrenner, M., Merkley, T.L., Santerre-Lemmon, L.E., Shamy, J.L., Skaggs, W.E., Buonocore, M.H., Rapp, P.R., Barnes, C.A., 2008. Age-related regional network of magnetic resonance imaging gray matter in the rhesus macaque. J. Neurosci. 28, 2710–2718. http://dx.doi.org/10.1523/jneurosci.1852-07.2008.

Alvarezroyo, P., Clower, R.P., Zolamorgan, S., Squire, L.R., 1991. Stereotaxic lesions of the hippocampus in monkeys - determination of surgical coordinates and analysis of lesions using magnetic-resonance-imaging. J. Neurosci. Methods 38, 223–232. http://dx.doi.org/10.1016/0165-0270(91)90172-V.

Baccala, L.A., Sameshima, K., 2001. Partial directed coherence: a new concept in neural structure determination. Biol. Cybern. 84, 463–474. http://dx.doi.org/10.1007/PI00007990.

Baker, S.N., Philbin, N., Spinks, R., Pinches, E.M., Wolpert, D.M., MacManus, D.G., Pauluis, Q., Lemon, R.N., 1999. Multiple single unit recording in the cortex of monkeys using independently moveable microelectrodes. J. Neurosci. Methods 94, 5–17.

Bakhurin, K.I., Mac, V., Golshani, P., Masmanidis, S.C., 2016. Temporal correlations among functionally specialized striatal neural ensembles in reward-conditioned mice. J. Neurophysiol. 115, 1521–1532. http://dx.doi.org/10.1152/jn.01037.2015.

Barua, N.U., Woolley, M., Bienemann, A.S., Johnson, D., Wyatt, M.J., Irving, C., Lewis, O., Castrique, E., Gill, S.S., 2013. Convection-enhanced delivery of AAV2 in white matter—A novel method for gene delivery to cerebral cortex. J. Neurosci. Methods 220, 1–8. http://dx.doi.org/10.1016/j.jneumeth.2013.08.011.

Bjarkam, C.R., Cancian, G., Glud, A.N., Ettrup, K.S., Jørgensen, R.L., Sørensen, J.-C., 2009. MRI-guided stereotaxic targeting in pigs based on a stereotaxic localizer box fitted with an isocentric frame and use of SurgiPlan computer-planning software. J. Neurosci. Methods 183, 119–126. http://dx.doi.org/10.1016/j.jneumeth.2009.06.019.

Buzsaki, G., 2004. Large-scale recording of neuronal ensembles. Nat. Neurosci. 7, 446–451. http://dx.doi.org/10.1038/nn1233.

Chen, L., Li, N., Gao, L., Yang, C., Fang, W., Wang, X.-l., Gao, G.-d., 2015. Improved stereotactic procedure enhances the accuracy of deep brain stimulation electrode implantation in non-human primates. Int. J. Neurosci. 125, 380–389. http://dx.doi.org/10.3109/00207454.2014.940524.

Chen, Y.H., Bressler, S.L., Ding, M.Z., 2006. Frequency decomposition of conditional granger causality and application to multivariate neural field potential data. J. Neurosci. Methods 150, 228–237. http://dx.doi.org/10.1016/j.jneumeth.2005.06.011.

Cunningham, J.P., Yu, B.M., 2014. Dimensionality reduction for large-scale neural recordings. Nat. Neurosci. 17, 1500–1509. http://dx.doi.org/10.1038/nn.3776.

Daye, P.M., Monosov, I.E., Hikosaka, O., Leopold, D.A., Optican, L.M., 2013. pyElectrode: an open-source tool using structural MRI for electrode positioning and neuron mapping. J. Neurosci. Methods 213 (1), 123–131. http://dx.doi.org/10.1016/j.jneumeth.2012.12.012.

Deogaonkar, M., Heers, M., Mahajan, S., Brummer, M., Subramanian, T., 2005. Method of construction of a MRI-based tabular database of 3D stereotaxic co-ordinates for individual structures in the basal ganglia of Macaca mulatta. J. Neurosci. Methods 149, 154–163. http://dx.doi.org/10.1016/j.jneumeth.2005.05.016.

Dubowitz, D.J., Scadeng, M., 2011. A frameless stereotaxic MRI technique for macaque neuroscience studies. Open Neuroimag. J. 5, 198–205. http://dx.doi.org/10.2174/1874440001105010198.

Fitzpatrick, J.M., West, J.B., Maurer, C.R., 1998. Predicting error in rigid-body point-based registration. IEEE Trans. Med. Imaging 17, 694–702. http://dx.doi.org/10.1109/42.736021.

Flesher, S.N., Collinger, J.L., Foldes, S.T., Weiss, J.M., Downey, J.E., Tyler-Kabara, E.C., Bensmaia, S.J., Schwartz, A.B., Boninger, M.L., Gaunt, R.A., 2016. Intracortical microstimulation of human somatosensory cortex. Sci. Transl. Med. http://dx.doi.org/10.1126/scitranslmed.aaf8083.

Francois, C., Yelnik, J., Percheron, G., 1996. A stereotaxic atlas of the basal ganglia in

macaques. Brain Res. Bull. 41, 151–158.
Frey, S., Comeau, R., Hynes, B., Mackey, S., Petrides, M., 2004. Frameless stereotaxy in the nonhuman primate. Neuroimage 23, 1226–1234. http://dx.doi.org/10.1016/j.neuroimage.2004.07.001.
Galashan, F.O., Rempel, H.C., Meyer, A., Gruber-Dujardin, E., Kreiter, A.K., Wegener, D., 2011. A new type of recording chamber with an easy-to-exchange microdrive array for chronic recordings in macaque monkeys. J. Neurophysiol. 105, 3092–3105. http://dx.doi.org/10.1152/jn.00508.2010.
Gilja, V., Nuyujukian, P., Chestek, C.A., Cunningham, J.P., Yu, B.M., Fan, J.M., Churchland, M.M., Kaufman, M.T., Kao, J.C., Ryu, S.I., Shenoy, K.V., 2012. A high-performance neural prosthesis enabled by control algorithm design. Nat. Neurosci. 15, 1752–1757. http://dx.doi.org/10.1038/nn.3265.
Gilja, V., Pandarinath, C., Blabe, C.H., Nuyujukian, P., Simeral, J.D., Sarma, A.A., Sorice, B.L., Perge, J.A., Jarosiewicz, B., Hochberg, L.R., Shenoy, K.V., Henderson, J.M., 2015. Clinical translation of a high-performance neural prosthesis. Nat. Med. 21, 1142–1145. http://dx.doi.org/10.1038/nm.3953.
Gray, C.M., Konig, P., Engel, A.K., Singer, W., 1989. Oscillatory responses in cat visual cortex exhibit inter-columnar synchronization which reflects global stimulus properties. Nature 338, 334–337. http://dx.doi.org/10.1038/338334a0.
Gutierrez, J., Lamanna, J.J., Grin, N., Hurtig, C.V., Miller, J.H., Riley, J., Urquia, L., Avalos, P., Svendsen, C.N., Federici, T., Boulis, N.M., 2015. Preclinical validation of multilevel intraparenchymal stem cell therapy in the porcine spinal cord. Neurosurgery 77, 604–612. http://dx.doi.org/10.1227/NEU.0000000000000882. discussion 612.
Hartov, A., Roberts, D.W., 2009. Accuracy in stereotactic and image guidance. In: Lozano, A.M., Gildenberg, P.L., Tasker, R.R. (Eds.), Textbook of Stereotactic and Functional Neurosurgery. Springer Berlin Heidelberg, Berlin, Heidelberg.
Henderson, J.M., 2009. Frameless functional stereotactic approaches. In: Bakay, R. (Ed.), Movement Disorder Surgery. Thieme Medical Publishers, Inc, New York, NY.
Hochberg, L.R., Bacher, D., Jarosiewicz, B., Masse, N.Y., Simeral, J.D., Vogel, J., Haddadin, S., Liu, J., Cash, S.S., van der Smagt, P., Donoghue, J.P., 2012. Reach and grasp by people with tetraplegia using a neurally controlled robotic arm. Nature 485, 372–375. http://dx.doi.org/10.1038/nature11076.
Hochberg, L.R., Serruya, M.D., Friehs, G.M., Mukand, J.A., Saleh, M., Caplan, A.H., Branner, A., Chen, D., Penn, R.D., Donoghue, J.P., 2006. Neuronal ensemble control of prosthetic devices by a human with tetraplegia. Nature 442, 164–171. http://dx.doi.org/10.1038/nature04970.
Jarosiewicz, B., Sarma, A.A., Bacher, D., Masse, N.Y., Simeral, J.D., Sorice, B., Oakley, E.M., Blabe, C., Pandarinath, C., Gilja, V., Cash, S.S., Eskandar, E.N., Friehs, G., Henderson, J.M., Shenoy, K.V., Donoghue, J.P., Hochberg, L.R., 2015. Virtual typing by people with tetraplegia using a self-calibrating intracortical brain-computer interface. Sci. Transl. Med. 7. http://dx.doi.org/10.1126/scitranslmed.aac7328.
Kaminski, M., Ding, M., Truccolo, W.A., Bressler, S.L., 2001. Evaluating causal relations in neural systems: granger causality, directed transfer function and statistical assessment of significance. Biol. Cybern. 85, 145–157.
Kaminski, M.J., Blinowska, K.J., 1991. A new method of the description of the information flow in the brain structures. Biol. Cybern. 65, 203–210. http://dx.doi.org/10.1007/bf00198091.
Katnani, H.A., Patel, S.R., Kwon, C.S., Abdel-Aziz, S., Gale, J.T., Eskandar, E.N., 2016. Temporally coordinated deep brain stimulation in the dorsal and ventral striatum synergistically enhances associative learning. Sci. Rep. 6, 18806. http://dx.doi.org/10.1038/srep18806.
Knight, E.J., Min, H.K., Hwang, S.C., Marsh, M.P., Paek, S., Kim, I., Felmlee, J.P., Abulseoud, O.A., Bennet, K.E., Frye, M.A., Lee, K.H., 2013. Nucleus accumbens deep brain stimulation results in insula and prefrontal activation: a large animal FMRI study. PLoS One 8, e56640. http://dx.doi.org/10.1371/journal.pone.0056640.
Koo, B.B., Schettler, S.P., Murray, D.E., Lee, J.M., Killiany, R.J., Rosene, D.L., Kim, D.S., Ronen, I., 2012. Age-related effects on cortical thickness patterns of the Rhesus monkey brain. Neurobiol. Aging 33, 200. http://dx.doi.org/10.1016/j.neurobiolaging.2010.07.010. e23-31.
Lee, S.R., Lee, H.J., Cha, S.H., Jeong, K.J., Lee, Y., Jeon, C.Y., Yi, K.S., Lim, I., Cho, Z.H., Chang, K.T., Kim, S.U., 2015. Long-term survival and differentiation of human neural stem cells in nonhuman primate brain with no immunosuppression. Cell Transpl. 24, 191–201. http://dx.doi.org/10.3727/096368914X678526.
Li, N., Gao, L., Wang, X.L., Chen, L., Fang, W., Ge, S.N., Gao, G.D., 2013. Deep brain stimulation of the bilateral nucleus accumbens in normal rhesus monkey. Neuroreport 24, 30–35. http://dx.doi.org/10.1097/WNR.0b013e32835c16e7.
Lin, L.N., Chen, G.F., Xie, K., Zaia, K.A., Zhang, S.Q., Tsien, J.Z., 2006. Large-scale neural ensemble recording in the brains of freely behaving mice. J. Neurosci. Methods 155, 28–38. http://dx.doi.org/10.1016/j.jneumeth.2005.12.032.
Maldonado, P.E., Friedman-Hill, S., Gray, C.M., 2000. Dynamics of striate cortical activity in the alert macaque: II. Fast time scale synchronization. Cereb. Cortex 10, 1117–1131.
Matochik, J.A., Chefer, S.I., Lane, M.A., Woolf, R.I., Morris, E.D., Ingram, D.K., Roth, G.S., London, E.D., 2000. Age-related decline in striatal volume in monkeys as measured by magnetic resonance imaging. Neurobiol. Aging 21, 591–598.
McBride, J.L., Clark, R.L., 2016. Stereotaxic surgical targeting of the nonhuman primate caudate and putamen: Gene therapy for Huntington's disease. In: Manfredsson, P.F. (Ed.), Gene Therapy for Neurological Disorders: Methods and Protocols. Springer New York, New York, NY.
McLaren, D.G., Kosmatka, K.J., Oakes, T.R., Kroenke, C.D., Kohama, S.G., Matochik, J.A., Ingram, D.K., Johnson, S.C., 2009. A population-average MRI-based atlas collection of the rhesus macaque. Neuroimage 45, 52–59. http://dx.doi.org/10.1016/j.neuroimage.2008.10.058.
Miocinovic, S., Zhang, J., Xu, W., Russo, G.S., Vitek, J.L., McIntyre, C.C., 2007. Stereotactic neurosurgical planning, recording, and visualization for deep brain stimulation in non-human primates. J. Neurosci. Methods 162, 32–41. http://dx.doi.org/10.1016/j.jneumeth.2006.12.007.
Pardo, I.D., Garman, R.H., Weber, K., Bobrowski, W.F., Hardisty, J.F., Morton, D., 2012. Technical guide for nervous system sampling of the cynomolgus monkey for general toxicity studies. Toxicol. Pathol. 40, 624–636. http://dx.doi.org/10.1177/0192623311436180.
Patil, P.G., Carmena, L.M., Nicolelis, M.A.L., Turner, D.A., 2004. Ensemble recordings of human subcortical neurons as a source of motor control signals for a brain-machine interface. Neurosurgery 55, 27–35. http://dx.doi.org/10.1227/01.Neu.0000126872.23715.E5.
Paxinos, G., Huang, X., Toga, A., 1999. The Rhesus Monkey Brain in Stereotaxic Coordinates. Academic Press, London, UK.
Perry, J.H., Rosenbaum, A.E., Lunsford, L.D., Swink, C.A., Zorub, D.S., 1980. Computed tomography/guided stereotactic surgery: conception and development of a new stereotactic methodology. Neurosurgery 7, 376–381.
Quiroga, R.Q., Panzeri, S., 2009. Extracting information from neuronal populations: information theory and decoding approaches. Nat. Rev. Neurosci. 10, 173–185. http://dx.doi.org/10.1038/nrn2578.
Rebert, C.S., Hurd, R.E., Matteucci, M.J., Delapaz, R., Enzmann, D.R., 1991. A procedure for using proton magnetic resonance imaging to determine stereotaxic coordinates of the monkey's brain. J. Neurosci. Methods 39, 109–113. http://dx.doi.org/10.1016/0165-0270(91)90076-C.
Riehle, A., Grun, S., Diesmann, M., Aertsen, A., 1997. Spike synchronization and rate modulation differentially involved in motor cortical function. Science 278, 1950–1953.
Saleem, K., Logothetis, N., 2012. A Combined MRI and Histology Atlas of the Rhesus Monkey Brain in Stereotaxic Coordinates. Academic Press, Boston, MA.
Saunders, R.C., Aigner, T.G., Frank, J.A., 1990. Magnetic resonance imaging of the rhesus monkey brain: use for stereotactic neurosurgery. Exp. Brain Res. 81, 443–446.
Selek, L., Seigneuret, E., Nugue, G., Wion, D., Nissou, M.F., Salon, C., Seurin, M.J., Carozzo, C., Ponce, F., Roger, T., Berger, F., 2014. Imaging and histological characterization of a human brain xenograft in pig: the first induced glioma model in a large animal. J. Neurosci. Methods 221, 159–165. http://dx.doi.org/10.1016/j.jneumeth.2013.10.002.
Sridharan, A., Rajan, S.D., Muthuswamy, J., 2013. Long-term changes in the material properties of brain tissue at the implant-tissue interface. J. Neural Eng. 10, 066001. http://dx.doi.org/10.1088/1741-2560/10/6/066001.
Thompson, E.M., Anderson, G.J., Roberts, C.M., Hunt, M.A., Selden, N.R., 2011. Skull-fixated fiducial markers improve accuracy in staged frameless stereotactic epilepsy surgery in children. J. Neurosurg. Pediatr. 7, 116–119. http://dx.doi.org/10.3171/2010.10.peds10352.
Walbridge, S., Murad, G.J.A., Heiss, J.D., Oldfield, E.H., Lonser, R.R., 2006. Technique for enhanced accuracy and reliability in non-human primate stereotaxy. J. Neurosci. Methods 156, 310–313. http://dx.doi.org/10.1016/j.jneumeth.2006.01.025.
White, E., Woolley, M., Bienemann, A., Johnson, D.E., Wyatt, M., Murray, G., Taylor, H., Gill, S.S., 2011. A robust MRI-compatible system to facilitate highly accurate stereotactic administration of therapeutic agents to targets within the brain of a large animal model. J. Neurosci. Methods 195, 78–87. http://dx.doi.org/10.1016/j.jneumeth.2010.10.023.